EARTH SURFACE PROCESSES AND LANDFORMS
Earth Surf. Process. Landforms **43**, 349–362 (2018)

Published online 14 August 2017 in Wiley Online Library
(wileyonlinelibrary.com) DOI: 10.1002/esp.4204

The influence of flow discharge variations on the morphodynamics of a diffluence–confluence unit on a large river

Christopher R. Hackney,[1]* Stephen E. Darby,[2] Daniel R. Parsons,[1] Julian Leyland,[2] Rolf Aalto,[3] Andrew P. Nicholas[4] and James L. Best[4]

[1] Geography and Geology, School of Environmental Sciences, University of Hull, Hull HU6 7RX, UK
[2] Geography and Environment, University of Southampton, Southampton SO17 1BJ, UK
[3] College of Life and Environmental Sciences, University of Exeter, Exeter EX4 4RJ, UK
[4] Departments of Geology, Geography and GIS, Mechanical Science and Engineering and Ven Te Chow Hydrosystems Laboratory, University of Illinois at Urbana-Champaign, Champaign, IL 61820, USA

Received 15 September 2016; Revised 21 April 2017; Accepted 13 July 2017

*Correspondence to: Christopher R. Hackney, Geography and Geology, School of Environmental Sciences, University of Hull, Hull HU6 7RX, UK. E-mail: c.hackney@hull.ac.uk

ESPL
Earth Surface Processes and Landforms

ABSTRACT: Bifurcations are key geomorphological nodes in anabranching and braided fluvial channels, controlling local bed morphology, the routing of sediment and water, and ultimately defining the stability of their associated diffluence–confluence unit. Recently, numerical modelling of bifurcations has focused on the relationship between flow conditions and the partitioning of sediment between the bifurcate channels. Herein, we report on field observations spanning September 2013 to July 2014 of the three-dimensional flow structure, bed morphological change and partitioning of both flow discharge and suspended sediment through a large diffluence–confluence unit on the Mekong River, Cambodia, across a range of flow stages (from 13 500 to 27 000 $m^3 s^{-1}$).

Analysis of discharge and sediment load throughout the diffluence–confluence unit reveals that during the highest flows ($Q = 27\,000\,m^3 s^{-1}$), the downstream island complex is a net sink of sediment (losing 2600 ± 2000 kg s^{-1} between the diffluence and confluence), whereas during the rising limb ($Q = 19\,500\,m^3 s^{-1}$) and falling limb flows ($Q = 13\,500\,m^3 s^{-1}$) the sediment balance is in quasi-equilibrium. We show that the discharge asymmetry of the bifurcation varies with discharge and highlight that the influence of upstream curvature-induced water surface slope and bed morphological change may be first-order controls on bifurcation configuration. Comparison of our field data to existing bifurcation stability diagrams reveals that during lower (rising and falling limb) flow the bifurcation may be classified as unstable, yet transitions to a stable condition at high flows. However, over the long term (1959–2013) aerial imagery reveals the diffluence–confluence unit to be fairly stable. We propose, therefore, that the long-term stability of the bifurcation, as well as the larger channel planform and morphology of the diffluence–confluence unit, may be controlled by the dominant sediment transport regime of the system. © 2017 The Authors. Earth Surface Processes and Landforms published by John Wiley & Sons Ltd.

KEYWORDS: bifurcation; discharge; large river; suspended sediment

Introduction

The passage of water and sediment through fluvial systems controls the evolution of channel planform, defines rates of channel adjustment and, over longer timescales, drives floodplain development and the construction of stratigraphy (Schumm, 1985; Aalto *et al.,* 2003, 2008; Constantine *et al.,* 2014). During its transit through the fluvial system, sediment may be stored in a range of in-channel landforms such as point or mid-channel bars, or during floods it can be deposited over banks onto islands and floodplains. Sediment may also be remobilized through bank erosion and the transfer of material from the floodplain into the channel. At larger spatial scales, it has been shown that channel planform attributes such as sinuosity and migration rate may be determined by sediment load and channel slope (Leopold and Wolman, 1957; Eaton *et al.,* 2010; Constantine *et al.,* 2014). However, the relationship between the rate at which sediment is supplied from the catchment upstream and the resulting imposed local channel morphology is spatially and temporally complex and it remains unclear how sediment dynamics through storage units modulate this larger-scale relationship.

The planform of large alluvial rivers has been observed to frequently tend towards an anabranching pattern (Latrubesse, 2008). Large rivers have also been shown to possess some of the highest global sediment loads (Milliman and Syvitski, 1992), with the 30 largest rivers between them contributing ~20% of the global sediment flux transmitted to the ocean

(Milliman and Farnsworth, 2011). Yet the passage of sediment and water through anabranching systems is complicated by the splitting and joining of the main channel around island and bar complexes (herein termed diffluence–confluence units). Diffluences, or bifurcations, are therefore key geomorphological nodes in anabranching channels, controlling local bed morphology, the routing of sediment and water, and ultimately defining the stability of diffluence–confluence units and channel planform (Bridge, 1993; Richardson and Thorne, 2001; Parsons *et al.,* 2007; Hardy *et al.,* 2011; Thomas *et al.,* 2011; Szupiany *et al.,* 2012; Kleinhans *et al.,* 2013).

Recent numerical modelling of bifurcations has focused on elucidating the relationship between flow conditions and the partitioning of sediment between bifurcate channels (Bolla Pittaluga *et al.,* 2003; Kleinhans *et al.,* 2008; Edmonds and Slingerland, 2008; Thomas *et al.,* 2011; Marra *et al.,* 2014). Much of this previous work has been concerned with coarse-grained bifurcating systems, with fine-grained systems receiving relatively less attention (Edmonds and Slingerland, 2008). This poses a problem when extrapolating bifurcation theory to the world's largest rivers, which are mostly fine-grained systems, although Bolla Pittaluga *et al*. (2015) have proposed a unified theory of bifurcation stability that seeks to link sediment transport equations for both coarse- and fine-grained bifurcations. Current models suggest that instability at a bifurcation may be initialized by positive feedback mechanisms associated with the distribution of water and sediment between two channels of unequal transport capacity (Bolla Pittaluga *et al.,* 2003), emphasizing the fundamental importance of secondary flow fields in controlling the distribution of flow and, more importantly, sediment between each branch of the bifurcation (Kleinhans *et al.,* 2008; Marra *et al.,* 2014).

In contrast to theoretical studies, field studies have thus far revealed a lack, or reduced significance, of secondary flow structures at bifurcations in large (i.e. anabranching) alluvial channels (McLelland *et al.,* 1990; Parsons *et al.,* 2007; Szupiany *et al.,* 2009, 2012). The apparent absence, or at least reduced significance, of secondary flow structures in such channels is likely due to the large width-to-depth ratios of natural (as opposed to their modelled cousins in flumes) large river channels, the associated reduction in cross-channel water surface slopes and the increasing role of form roughness, which acts to increase turbulence (Parsons *et al.,* 2007). These observations raise questions as to the extent to which theories that invoke the significance of secondary flow structures in modulating the partitioning of sediment in large river bifurcations actually apply (Szupiany *et al.,* 2012). Indeed, work by Szupiany *et al*. (2012) highlights other factors as being key to understanding the distribution of suspended sediments, and ultimately morphological changes, within a large river bifurcation. These characteristics, namely flow distribution, suspended sediment transport, bed shear stress and bed material grain size, will all vary to some degree as a function of varying flow discharge. However, no field studies have yet been conducted that examine the role of bifurcation dynamics across a range of flow discharges in large rivers, even though many such large rivers have highly seasonal flow regimes. It thus follows that, in order to better understand the stability and dynamics of large river bifurcations, and thus the morphodynamics of large river channel planforms, empirical studies that assess the distribution of water and sediment flux through the discrete branches of diffluence–confluence units, and across a range of flow discharges, are required.

In this paper we report findings from a study into the partitioning of flow and suspended sediment at a bifurcation of a diffluence–confluence unit within a fine-grained, anabranching, reach of the Mekong River. Field surveys were conducted on the rising, flood and falling stages of the annual monsoonal flood pulse, providing new insight into the dynamics of a large river diffluence–confluence unit across a range (13 500–27 000 $m^3 s^{-1}$) of flow discharges. We detail the dynamics and structure of the variable flows within the bifurcation, before describing the morphodynamics of the bed at the upstream bifurcation and identifying local storages and sources of suspended sediment through the larger diffluence–confluence unit. This new field dataset adds to the existing body of literature on large sand-bed river bifurcations within anabranching systems and, importantly, provides the first field-based contextualization of the role that variations in flow discharge play in the distribution and dynamics of water and sediment within a large river diffluence–confluence unit.

Study Site and Methodology

Study site

The Mekong River is one of the world's largest, ranking 12th in terms of its length (~4900 km) and 27th in terms of drainage area (816 000 km^2; Kummu *et al.,* 2008). The Mekong has an estimated mean annual sediment load of 87.4 ± 28.7 Mt a^{-1} (Darby *et al.,* 2016) and mean annual runoff of 475 km^3 (MRC, 2009). The Mekong's hydrology is dominated by single wet-season flow peaks associated with the passage of the East Asian and Indian monsoons (Adamson *et al.,* 2009; Darby *et al.,* 2013). The mean annual flow (1960–2002) at Kampong Cham, Cambodia, is 14 500 $m^3 s^{-1}$, but with an average flood discharge of 52 500 $m^3 s^{-1}$. Upstream of the town of Kratie, Cambodia, the Mekong is largely controlled by bedrock (Gupta and Liew, 2007; Carling, 2009), such that its planform migration and channel geometry are highly constrained (Kummu *et al.,* 2008; Hackney and Carling, 2011). South of Kratie, and upstream of the apex of its delta at Phnom Penh, expansive floodplains have developed, allowing the unconstrained Mekong to migrate freely across largely Quaternary alluvium with characteristic anabranching and anastomosed channels developing (Carling, 2009). The area that is the focus of this study, comprising a large asymmetrical bar bifurcation (see Figure 1A), is located ~2 km south of the city of Kampong Cham, within the anabranching reach. Bed material was sampled using an Ekman grab sampler at three locations evenly spaced across the channel at the head of the bifurcation (XS001) and during each survey period. The bed material in this reach was found to be predominantly fine to medium sand, but it coarsened during the higher flows observed in September 2013 (D_{50} = 0.4 mm, October 2013 and July 2014; 2 mm, September 2013).

Surveys of flow, river bed bathymetry and suspended sediment concentrations (see section below for details) were undertaken at three flow discharges corresponding to different stages of the annual flood pulse (Figure 1B): (i) a 'rising limb' survey was conducted in July 2014 when the discharge was 19 500 $m^3 s^{-1}$; (ii) a 'peak flood' survey was conducted in September 2013 at a discharge of 27 000 $m^3 s^{-1}$; and (iii) the 'falling limb' survey was undertaken at the end of October 2013, when flow discharge had reduced to 13 500 $m^3 s^{-1}$.

Bathymetric surveys and flow mapping

High-resolution multibeam echo sounding (MBES) surveys were conducted at the upstream bifurcation (see Figure 1A for location) to provide detailed bathymetry at the major bifurcation node. We employed a RESON SeaBat 7125 system operating at 400 kHz and forming 512 equal-angle beams across a 140° swathe. A Leica 1230 differential global positioning system

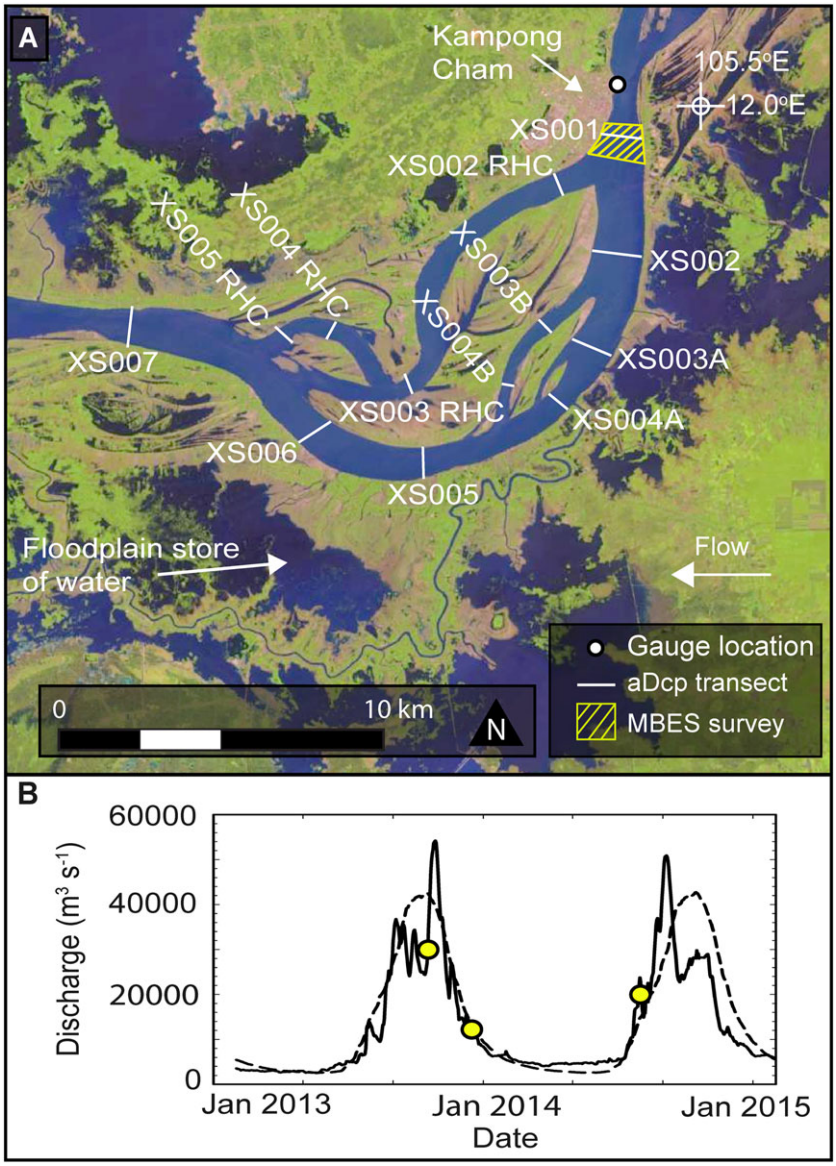

Figure 1. (A) Landsat 8 image (October 2013) showing the island complex at Kampong Cham with the location of the acoustic Doppler current profiler cross-sections (white lines) and multi-beam echo sounder survey area (yellow checked box). The location of the Kampong Cham gauge is shown by the white filled circle. (B) Hydrograph from Kampong Cham, Cambodia, for 2013 and 2014 (solid lines) superimposed on the 1960–2002 mean annual hydrograph for the same station (dashed lines) with the timings of the three surveys (yellow filled circles). [Colour figure can be viewed at wileyonlinelibrary.com]

(dGPS) was used to provide position with accuracy to ±0.02 m and ±0.03 m in the horizontal and vertical, respectively. The dGPS was coupled to an Applanix POS-MV WaveMaster inertial motion unit (IMU), which also provided full, real-time, three-dimensional (3-D) motion and heading data correction for the MBES, along with synchronization of all survey data streams using the dGPS time stamp and a pulse per second (PPS) signal. Post-survey calibration and correction for angular offsets and the application of sound velocity corrections were applied to the MBES data within CARIS-HIPS (v.9) software.

Detailed 3-D time–mean flow velocity fields were obtained around the diffluence–confluence unit using a series of acoustic Doppler current profilers (aDcp). Owing to instrument availability and the flow conditions at the time of the survey, we employed two RDI Teledyne RioGrande 600 kHz and one RDI Teledyne RioGrande 1200 kHz units. Flow measurements were made at a series of predetermined cross-sections (Figure 1B). At each cross-section, multiple repeat surveys were undertaken to resolve the time-averaged flow field (Szupiany *et al.,* 2007). At major cross-sections where analysis of the 3-D flow structures was undertaken, four passes were obtained (XS001 and XS007; Figure 1). At all other transects, where only discharge and suspended sediment flux was calculated, two passes per cross-section were made. Each aDcp unit was coupled to the same RTK dGPS used in the MBES surveys to determine the position and velocity of the survey vessel. Following Szupiany *et al.* (2007), boat speed and trajectory were constantly monitored during the survey to reduce associated errors. The primary and secondary flow structures (if present) at each cross-section were processed using the Velocity Mapping Toolbox (VMT; Parsons *et al.,* 2013) and were defined using a zero net cross-stream discharge decomposition (Lane *et al.,* 2000).

Suspended sediment concentration and suspended sediment flux

Previous work has shown that suspended sediment concentration as measured at-a-point in a cross-section can be estimated using the corrected acoustic backscatter value recorded by the aDcp at the same location (Kostaschuk *et al.,* 2005; Szupiany *et al.,* 2009; Shugar *et al.,* 2010). This relationship is based on

the assumption that the intensity of the acoustic backscatter recorded by the aDcp is a function not only of equipment characteristics but also water column conditions (i.e. the concentration and size of suspended sediment therein). Therefore, for a given instrument and for a given sediment type and sediment size distribution, a simple relationship between acoustic backscatter and sediment concentration should be obtainable (Szupiany *et al.,* 2009).

Following Szupiany *et al.* (2009), we corrected the echo intensity values recorded by the aDcp using the simplified sonar equation:

$$\mathrm{EL} = \mathrm{SL} + 10\log_{10}(\mathrm{PL}) - 20\log_{10}(R) - 2\alpha_s R + S_v + \mathrm{RS} \quad (1)$$

where EL is the signal intensity recorded by the aDcp, PL, SL and RS are determined solely by the individual instrument characteristics, R is the distance between the aDcp transducer and the measured volume, α_s is the sound absorption coefficient, and S_v is the volume scattering strength. To provide a measure of suspended sediment concentrations with which to regress the recorded acoustic backscatter signal, we collected point samples using a 3 L Van Dorn (Rutner) sampler at three evenly spaced verticals across the channel and at three points within each vertical profile. These point samples were obtained across a variety of flow conditions and locations such that we were able to produce unique calibration curves specific to each of the three aDcp units employed in this study (Figure 2). The range of suspended sediment concentrations covered by the sampling procedure was 6–531 mg L^{-1}. Simultaneous aDcp measurements were taken to enable direct comparison between the directly measured suspended sediment concentrations and the recorded acoustic backscatter. The resultant calibration curves (Figure 2) display high correlations that are significant at 95% confidence levels (with R^2 values of 0.83, 0.87 and 0.67, for the two 600 kHz units and the 1200 kHz unit, respectively). Using these relationships, along with the flow velocity field across each aDcp survey transect, we then estimated fluxes of suspended sediment at each location. Specifically, for each cross-section transect, the acoustic backscatter values were converted to a suspended sediment concentration using the appropriate calibration curve. The associated velocity measurements from the aDcp were then used to convert these concentrations into a mass flux at each cell, and finally these were integrated out across each cross-section to provide an instantaneous section-averaged suspended sediment load (kg s^{-1}).

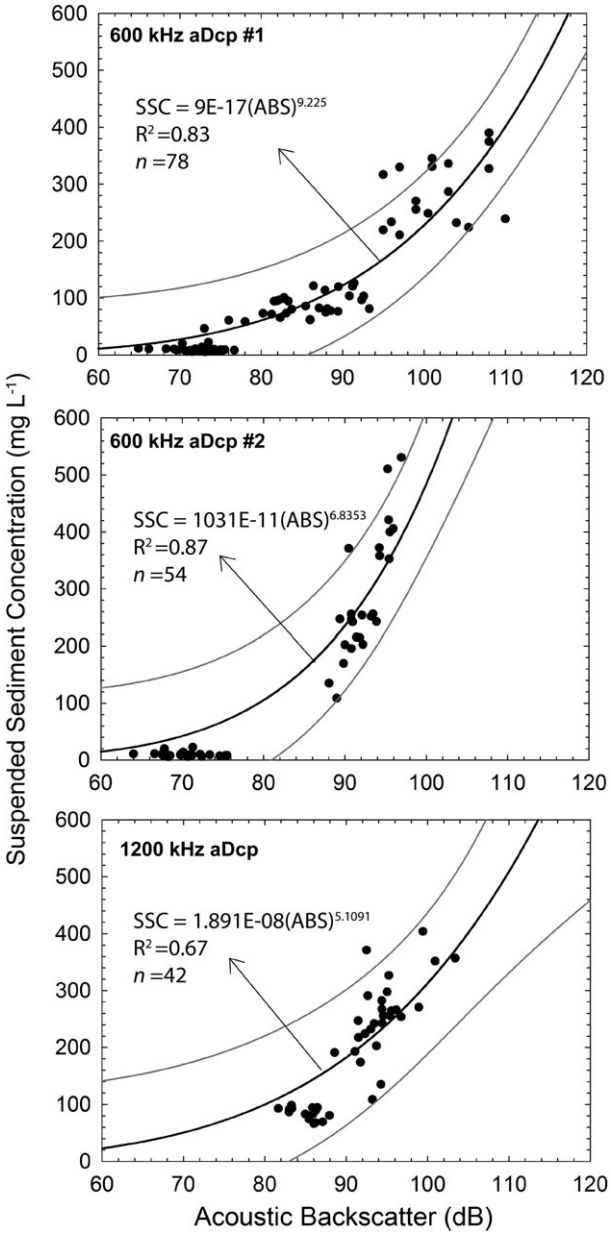

Figure 2. Relationships between corrected acoustic backscatter (dB) and measured suspended sediment concentration (mg L^{-1}) for the three aDcp units used in the study. 95% prediction bounds are shown in grey. For all fits, $P < 0.05$.

Bifurcation Dynamics

To understand the role that flow discharge variations play on the functioning of a large river bifurcation and the effects of such variations on the diffluence–confluence unit downstream of the bifurcation, we first report the hydrodynamic, sediment transport and morphological variability observed at the bifurcation apex across the three observed flow discharges. We then discuss how the partitioning of water and suspended sediment through the diffluence–confluence unit varies as a function of flow discharge.

Hydrodynamics of a large river bifurcation

Figure 3 displays the primary flow velocities (coloured map) and secondary flow vectors (zero net cross-stream discharge decomposition; arrows) derived from the aDcp surveys conducted at XS001 (Figure 1A), the transect located at the bifurcation head, during each of the three field surveys. During the rising limb (July 2014, $Q = 19\,500\ \mathrm{m^3\,s^{-1}}$), the depth-averaged cross-sectional velocity (U) was 0.98 m s^{-1}, during the highest discharges (September 2013, $Q = 27\,000\ \mathrm{m^3\,s^{-1}}$) $U = 1.14$ m s^{-1}, whereas during the falling limb (October 2013, $Q = 13\,500\ \mathrm{m^3\,s^{-1}}$) $U = 0.7$ m s^{-1}. As can be seen in Figure 3, during the rising and falling limbs of the flood wave the high-velocity core is confined within the centre of the channel, with downstream flow velocities decreasing towards either bank. On the rising limb (July 2014) the high-velocity core (defined as the area of flow where the ratio of observed flow to mean cross-section flow is greater than or equal to 1.5) comprises only 3% of the total area of the channel. During the falling limb (October 2013) the high-velocity core comprises 10% of the channel, whereas during the high discharge event of September 2013 the high-velocity core occupies 8% of the channel cross-sectional area. Although flow velocity decreases towards the banks during September 2013, flows of 1.2 m s^{-1} and greater are found within approximately 200 m from the banks. During the falling limb (October 2013), such velocities are found only

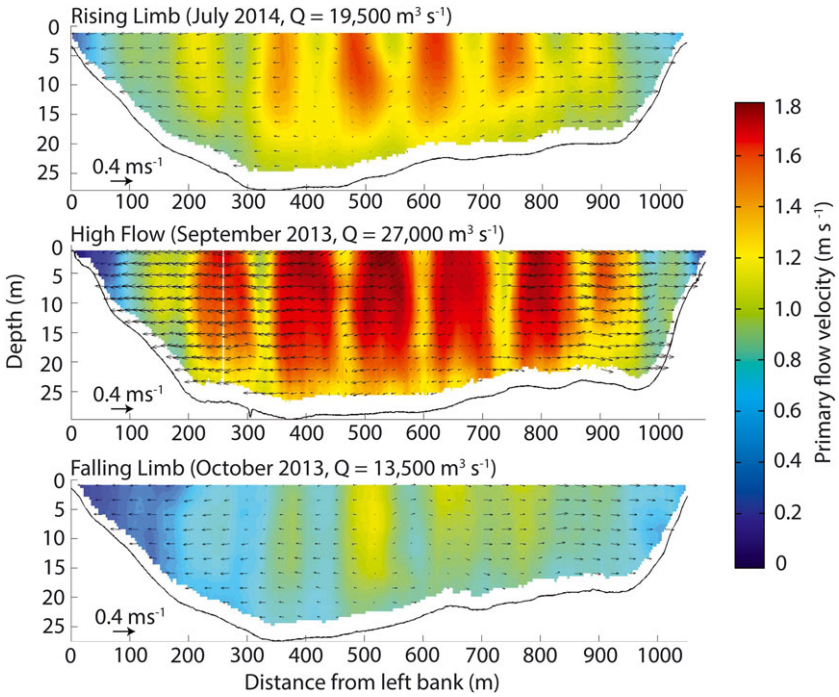

Figure 3. Primary flow velocities with secondary flow vectors for each of the three surveys conducted at the bifurcation head (XS001; Figure 1A). Data were collected using a 600 kHz aDcp. The vertical 'stripes' evident in the data represent the presence of bridge piers located ~200 m upstream of the survey line. [Colour figure can be viewed at wileyonlinelibrary.com]

in the high-velocity core, approximately 500 m from the banks (Figure 3). At higher flows, there is less variation in high velocities across the channel, making it less likely for spatial variations in suspended sediment concentration to occur within the channel cross-section.

The secondary flow velocity vectors plotted in Figure 3 also reveal that, during all three surveys, flow is directed outwards from the centre of the channel towards both banks. Figure 3 also shows that there is little to no exchange of flow in the vertical at these flow stages. That is to say, flow is predominantly being steered laterally to the left and right banks, and thus down the left and right hand channels of the bifurcation, without forming secondary flow cells. This is not surprising given that fully defined helical, secondary flow may be caused by either the interactions between centrifugal and pressure gradient forces or the heterogeneity and anisotropy of turbulence (Parsons *et al.,* 2007). In large rivers, the large width: depth ratios tend to reduce the influence of cross-stream water surface slopes, dampening the development of secondary flow cells. It is clear, however, that the location of the shear layer marking the divergence in flow shifts across the channel with changing flow discharge. During the rising limb (July 2014) the divergence occurs ~500 m from the left-hand bank. During high flows (September 2013) the divergence occurs ~725 m from the left-hand bank, while during the falling limb (October 2013) the secondary flow diverges ~520 m from the left-hand bank. This implies that during higher flows the flow field at the diffluence becomes more asymmetrical, with greater volumes of water being directed down the left-hand channel of the bifurcation (this is discussed further below).

Analysis of the cross-stream water surface elevations (recorded on average at a ~ 2.5 m spacing across the channel width) derived from the dGPS elevations recorded while conducting the MBES surveys during the different flow discharges (Figures 4A and 4B) reveals that, during the highest discharges (September 2013), the mean cross-stream water surface slope, calculated as the difference between the water surface elevations at the left- and right-hand bank divided by the cross-stream distance is 8×10^{-5} m m^{-1}, reducing to 3×10^{-5} m m^{-1} during the falling limb (October 2013), with a similar value of 4×10^{-5} m m^{-1} observed during the rising limb (July 2014) flow. It is noted here that the highest water surface elevations reported in Figure 4 are on the left hand bank. The planform of the main channel upstream of the survey area is that of a left turning bend, such that the highest water surface elevations may be expected to be found on the outer, right-hand bend. However, the presence of a constriction in the main channel ~1.2 km upstream of the survey location evidently deflects the high-velocity core towards the left-hand bank. This is visible in the MBES data reported in Figure 5, where the greatest depths are seen towards the left-hand bank. This topographic flow steering explains how flow is forced towards the left-hand bank, raising water surface elevations there, and likely plays a key role in conditioning the hydrodynamics at this bifurcation. As can be seen in Figure 4A, the strength and effect of this steering are reduced during lower flows. The impact of upstream curvature on discharge partitioning at bifurcations has long been recognized (Kleinhans *et al.,* 2008; Thomas *et al.*, 2011; Marra *et al.*, 2014), with lower cross-stream water surface slopes (i.e. less water being forced towards one bank or another), resulting in a more even distribution of flow within the channel.

In addition to the role of cross-stream water surface slope, both inertial effects and secondary flow have previously been shown to control discharge partitioning at bifurcations in large rivers (Parsons *et al.,* 2007; Szupiany *et al.,* 2012). Accordingly, for each of the surveys conducted here, we defined the dimensionless strength of the secondary flow component relative to the primary flow velocity, U_{s*}, following Blanckaert (2009):

$$U_{s*} = \sqrt{\left\langle (v_n - u_n)^2 \right\rangle} / U \tag{2}$$

where $(v_n - u_n)$ is the depth-averaged transverse velocity component of the curvature-induced secondary flow and U is

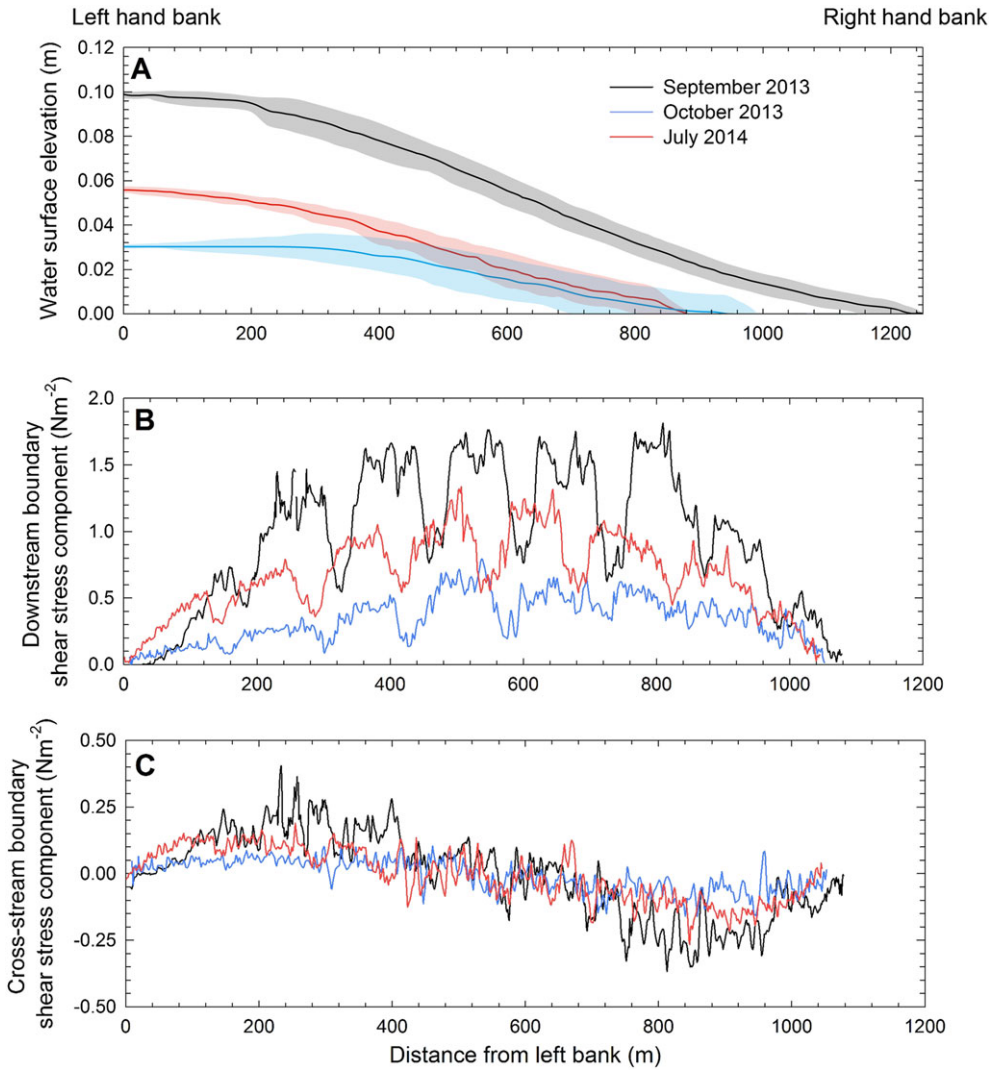

Figure 4. (A) Water surface elevations relative to the water elevation at the right-hand bank across the cross-section at the head of the bifurcation (XS001; Figure 1A) of September 2013 ($Q = 27\ 000\ m^3\ s^{-1}$; black line), October 2013 ($Q = 13\ 500\ m^3\ s^{-1}$; blue line) and July 2014 ($Q = 19\ 500\ m^3\ s^{-1}$; red line). The data are derived from dGPS data collected during the MBES surveys around the bifurcation head averaged at 2.5 m intervals across the channel (cross-hatched box; Figure 1A). The shaded areas represent 2 standard deviations in the average water surface elevation at each point across the channel. (B) The downstream component of the boundary shear stress as derived from Equations (3)–(5) and flow velocity data from the aDcp transect at XS001. (C) The cross-stream component of the boundary shear stress as derived from Equations (3)–5 and flow velocity data from the aDcp transect at XS001.Positive cross-stream shear stresses denote a vector towards the left-hand bank; negative shear stresses denote a vector towards the right-hand bank. The undulations in panels (B) and (C) are due to the location of the transect near bridge piers, and are reflected in the velocity profiles in Figure 3. [Colour figure can be viewed at wileyonlinelibrary.com]

the depth-averaged velocity. Using Equation (2), when the cross-stream water surface slope is at its lowest (3×10^{-5} m m^{-1}; October 2013, $Q = 13\ 500\ m^3\ s^{-1}$), the secondary flow strength is estimated to have a value of $U_{s^*} = 0.06$. At the highest cross-stream water surface slope (8×10^{-5} m m^{-1}; September 2013, $Q = 27\ 000\ m^3\ s^{-1}$), the estimated value of U_{s^*} decreased to 0.03, whereas it rose again to a value of 0.04 during July 2014 ($Q = 19\ 500\ m^3\ s^{-1}$), when the cross-stream water surface slope was 4×10^{-5} m m^{-1}. These data show that the observed increase in depth-averaged primary flow velocities is proportionally greater than the secondary flow component as the flow discharge increases. It is therefore likely that inertial effects have a greater effect on the distribution of water and sediment at this bifurcation during lower discharges, when the secondary flow is relatively stronger. Conversely, at the peak flow discharge, it appears that upstream, curvature-induced, forcing is the main control on water and sediment distribution through the bifurcation (discussed further below).

The above reported variations in flow velocity, cross-stream water surface elevation and secondary flow strength impact upon the boundary shear stress, τ_b, which in turn affects bed material transport capacity. Here, we estimate boundary shear stress using the Manning–Strickler law of bed resistance:

$$\tau_b = \rho C_f U^2 \tag{3}$$

where ρ is the fluid density and C_f is the coefficient of friction computed using

$$C_f = \left[\alpha_r \left(\frac{H}{k_s}\right)^{1/6}\right]^{-2} \tag{4}$$

where H is the mean flow depth, $\alpha_r$is set as 8.1 (Parker, 1991), and k_s is equal to $2.95D_{84}$ (here $D_{84} = 2.7$ mm in September 2013 and 0.5 mm in October 2013 and July 2014) as specified by Whiting and Dietrich (1990). Equation (3) can be generalized as a two-dimensional vector with streamwise (τ_{bu}) and cross-stream (τ_{bv}) component magnitudes of

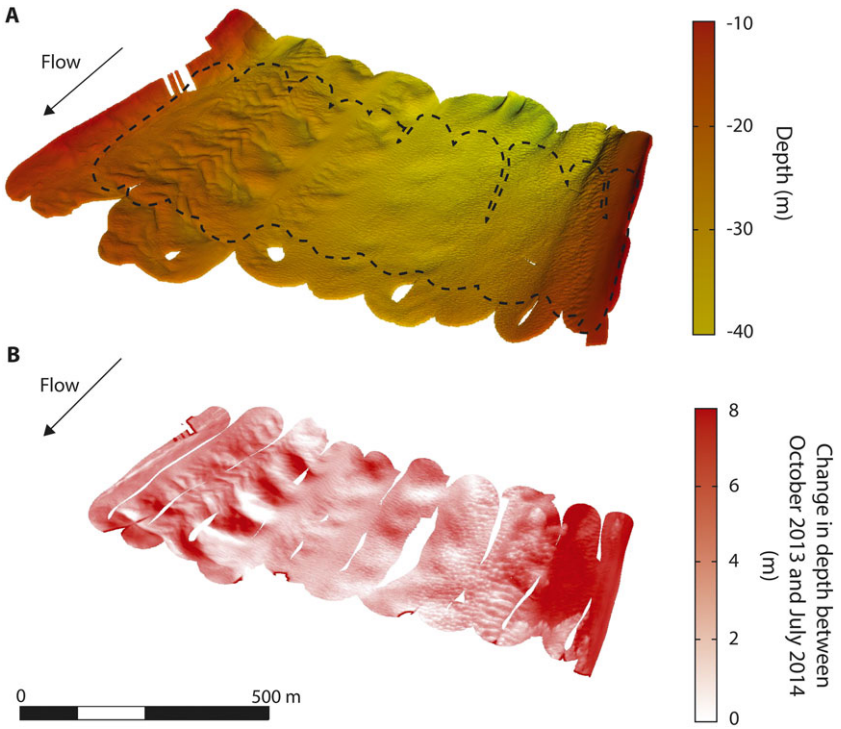

Figure 5. (A) MultiBeam echo sounder bathymetry for October 2013. Dashed line represents area of repeat survey undertaken in July 2014. (B) DEM of difference between July 2014 and October 2013. Scale bar applies to both panels. Flow is from top to bottom in each panel. [Colour figure can be viewed at wileyonlinelibrary.com]

$$\tau_{bu} = \rho C_f U\sqrt{U^2 + V^2}$$
$$\tau_{bv} = \rho C_f V\sqrt{U^2 + V^2} \quad (5)$$

where V is the depth-averaged cross-stream velocity following Engel and Rhoads (2016).

As can be seen in Figure 4B, bed shear stresses increase towards the centre of the channel during all three surveys, with the peaks in boundary shear corresponding to the locations of the high velocity cores shown in Figure 3. Greater values of τ_{bu} are experienced during the higher flow conditions in September 2013 ($Q = 27{,}000\,m^3\,s^{-1}$), where values reach a maximum of $1.5\,N\,m^{-2}$ in the centre of the channel, decreasing rapidly towards the channel margins. By comparison, the peak boundary shear stress during October 2013 ($Q = 13{,}500\,m^3\,s^{-1}$) is $0.6\,N\,m^{-2}$ and the variation across the channel is much more subdued, with a gradual decline towards the margins. During July 2014 ($Q = 19{,}500\,m^3\,s^{-1}$), the peak τ_{bu} was $1.4\,N\,m^{-2}$ but fairly high τ_{bu} values of $\sim 0.5\,N\,m^{-2}$ persist to within 200 m of the channel banks. Thus, despite their lower magnitudes, the distribution of bed shear stresses is much more even across the channel during the rising and falling limbs of the flood than during the highest flow discharge observed in this study.

By examining the cross-stream component of the bed shear stress, we are able to infer the potential direction of bedload transport at the apex of the bifurcation given the sign of τ_{bv}. Positive τ_{bv} indicates shear stresses directed towards the left bank, whereas negative τ_{bv} values indicate shear stresses directed towards the right bank. Figure 4C shows that the highest magnitudes of τ_{bv} occur during the highest discharges in September 2013 ($Q = 27{,}000\,m^3\,s^{-1}$), with the lowest magnitudes of τ_{bv} during October 2013 ($Q = 13{,}500\,m^3\,s^{-1}$). In the centre of the channel, between 400 to 700 m from the left-hand bank, the magnitude of τ_{bv} is negligible across all three surveys. Consequently, during all the flow discharges observed here, bed shear stress is directed predominantly in the downstream direction in the central portion of the channel. However, in a zone located at a distance of between 0 to 400 m from the left-hand bank, bed shear stress is clearly directed towards the left-hand bank during the high ($\tau_{bv} = 0.28\,N\,m^{-2}$; September 2013, $Q = 27{,}000\,m^3\,s^{-1}$) and rising limb ($\tau_{bv} = 0.16\,N\,m^{-2}$; July 2014, $Q = 19{,}500\,m^3\,s^{-1}$) flows, whereas during the falling limb flow there is a negligible cross-stream component of boundary shear stress. Conversely, in the zone located from 700 m to 1100 m from the left bank, boundary shear stress is directed toward the right-hand bank. Magnitudes of $-0.3\,N\,m^{-2}$ (where the negative sign defines the shear stress being directed from left to right) during the September 2013 high flow and $-0.22\,N\,m^{-2}$ during the July 2014 rising limb flow, indicate that the magnitude of boundary shear stress directed towards the right bank is greater than the boundary shear directed towards the left bank during the same flows. Even during the falling limb, the highest positive τ_{bv} magnitude observed ($0.08\,N\,m^{-2}$) is smaller than the highest negative τ_{bv} magnitude observed ($-0.15\,N\,m^{-2}$). This implies that the greatest sediment transport capacities are located within the right-hand portion of the channel.

Bed morphodynamics of a large river bifurcation

It has been shown in previous research that deposition and erosion in bifurcate channels impact upon the transverse bed slope that may steer discharge and sediment down the deeper, dominant channel (Bolla Pittaluga *et al.*, 2003; Kleinhans *et al.*, 2008; Marra *et al.*, 2014). Over the three surveys conducted in this study, morphological changes of the bed were revealed through MBES surveys of the bifurcation. As can be seen in Figure 5, these MBES surveys reveal net deposition of the bed of up to 8 m in places over the period October 2013 to July 2014. The areas of greatest deposition occur at the margins of the channel. It is in these areas that bed shear stresses are at their lowest (Figure 4B). In the central section of the channel, there is little (<1 m) deposition, which can be explained by bedform migration and translation during this period rather than systematic sediment accumulation on the bed. It is in this section where bed shear stresses have been shown to be at their

greatest (Figure 4B). The absence of erosion here implies that there is sufficient incoming sediment transported as bedload through this reach to maintain the bed topography at the upstream extent of the bifurcation throughout the period monitored.

Implications for the Diffluence–Confluence Unit

A network of aDcp surveys through the branches of the diffluence–confluence unit downstream of the bifurcation (Figure 1A) allows examination of the role that flow discharge variations plays in controlling the hydrodynamics and morphodynamics of a large river bifurcation and, in particular, the effect this has in defining the partitioning of flow discharge and suspended sediment around the downstream island complex. Such analysis is important because the flows of sediment and water around the island complex define the mobility of the island and thus impact upon the stability of the bifurcation and overall channel planform. Henceforth, the left (main) channel of the bifurcation will be termed C_1, while the right (subsidiary) channel will be termed C_2.

On the rising limb of the monsoon flood (July 2014; $Q = 19\,500\,m^3\,s^{-1}$), there was a net loss of $500 \pm 3850\,m^3\,s^{-1}$ (~3% of the total discharge; where the error estimate quoted equates to the summed errors of the water flux estimated at XS001 and XS007) between the apex of the bifurcation and the downstream confluence (Figure 6). This transmission loss lies within the error associated with the discharge estimates derived from aDcp units, here defined as one standard deviation of the individual discharge estimates of the four repeat transects taken at XS001 during all three surveys. Note that this one standard deviation estimate equates to roughly 10% of the combined discharge estimate, which is somewhat higher than previous estimates of aDcp error (5%; Mueller and Wagner, 2009). At high flows (September 2013; $Q = 27\,000\,m^3\,s^{-1}$), a net transmission loss of $1500 \pm 5250\,m^3\,s^{-1}$ was observed between the upstream bifurcation and downstream confluence (Figures 6C and 6D). This loss (~6%) is greater than that during the rising

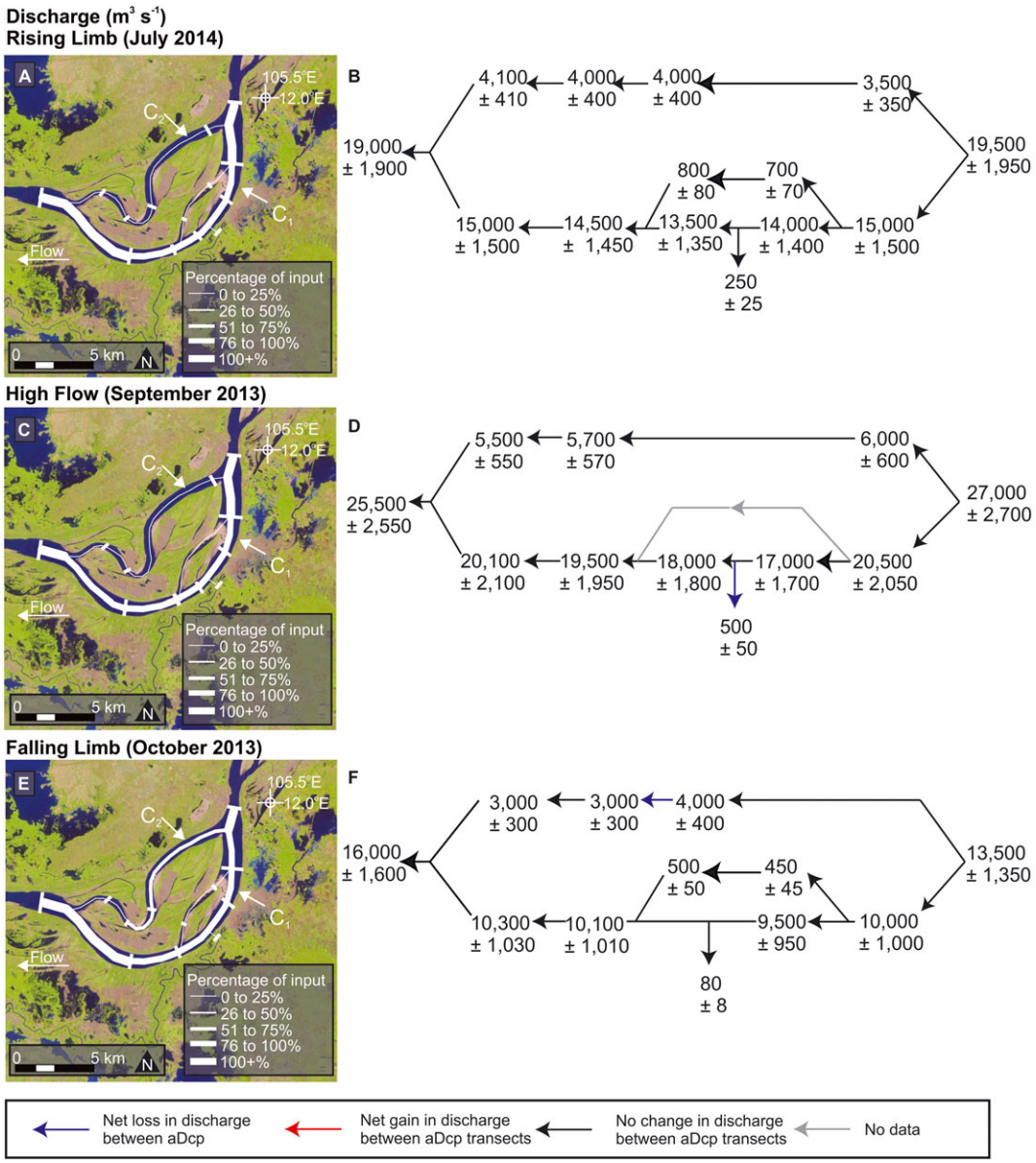

Figure 6. Discharge ($m^3\,s^{-1}$) fluctuations through the diffluence–confluence unit. (A, C, E) Flow diagrams with line widths proportional to the discharge measured at XS001 (upstream extent) overlain on Landsat 8 imagery from October 2013. (B, D, F) Topological representations of discharge through the diffluence–confluence unit on the rising limb, high flows and falling limbs, respectively. Links with gains (red), losses (blue), no change (black) and no data (grey) are identified. Errors provided are 10% of the value, equivalent to 1 standard deviation of the repeat transects taken at XS001. The large arrows beneath subplots (B), (D) and (F) represent links with significant gains (red) or losses (blue) where appropriate. [Colour figure can be viewed at wileyonlinelibrary.com]

stage but, however, still falls between the summative errors to XS001 and XS007 and so can be said to be in balance. Within the individual links of the bifurcation unit, the biggest loss of discharge can be identified as occurring between XS002 and XS003A in C_1, with a net loss of $3500 \pm 3750\,m^3\,s^{-1}$ (Figure 6D). Analysis of levee heights extracted from the Shuttle Radar Topography Mission (SRTM) 90 m spatial resolution elevation data around the outer banks of C_1 and C_2 reveals that at this flow stage water levels (measured at 14 m above Ha Tien datum at Kampong Cham) begin to overtop the levee crests down C_1, resulting in a transfer of water from the main channel onto the floodplain accounting for the loss of water seen in this link. Immediately below this link is an off-take channel through which a further $500 \pm 50\,m^3\,s^{-1}$ (based on direct aDcp survey) is lost.

During the falling limb of the hydrograph (October 2013; $Q = 13\,500\,m^3\,s^{-1}$), a net gain of $2500 \pm 2950\,m^3\,s^{-1}$ is apparent between the head and tail of the island complex (Figures 6E and 6F). The greatest influx of flow discharge occurs towards the end of the reach around the confluence zone, where C_1 and C_2 rejoin just upstream of XS007. Here, an additional $2700 \pm 2930\,m^3\,s^{-1}$ was recorded by the aDcp. Satellite imagery from the approximate date of this survey (Landsat, 8 October 2013, Julian day 297) reveals there is a large store of water present on the floodplain in close proximity to this region (see region of water on floodplain south of XS006 shown on Figure 1A). It is therefore likely that, as the main channel stage fell, flood waters stored on the floodplain were transferred back to the main channel due to the increased hydraulic gradient between the floodplain and channel.

During the rising limb, the suspended sediment flux recorded upstream of the bifurcation was $2150 \pm 430\,kg\,s^{-1}$. For suspended sediment estimates, we assume an error of 20% which equates to one standard deviation of the flux estimates derived from the four individual transect passes at XS001 across all three survey seasons. At the downstream limit of the reach, the load recorded was $2000 \pm 400\,kg\,s^{-1}$; thus a loss of $150 \pm 830\,kg\,s^{-1}$ (12%) occurred across the unit at this flow stage. As can be seen in Figures 7A and 7B, approximately 1500

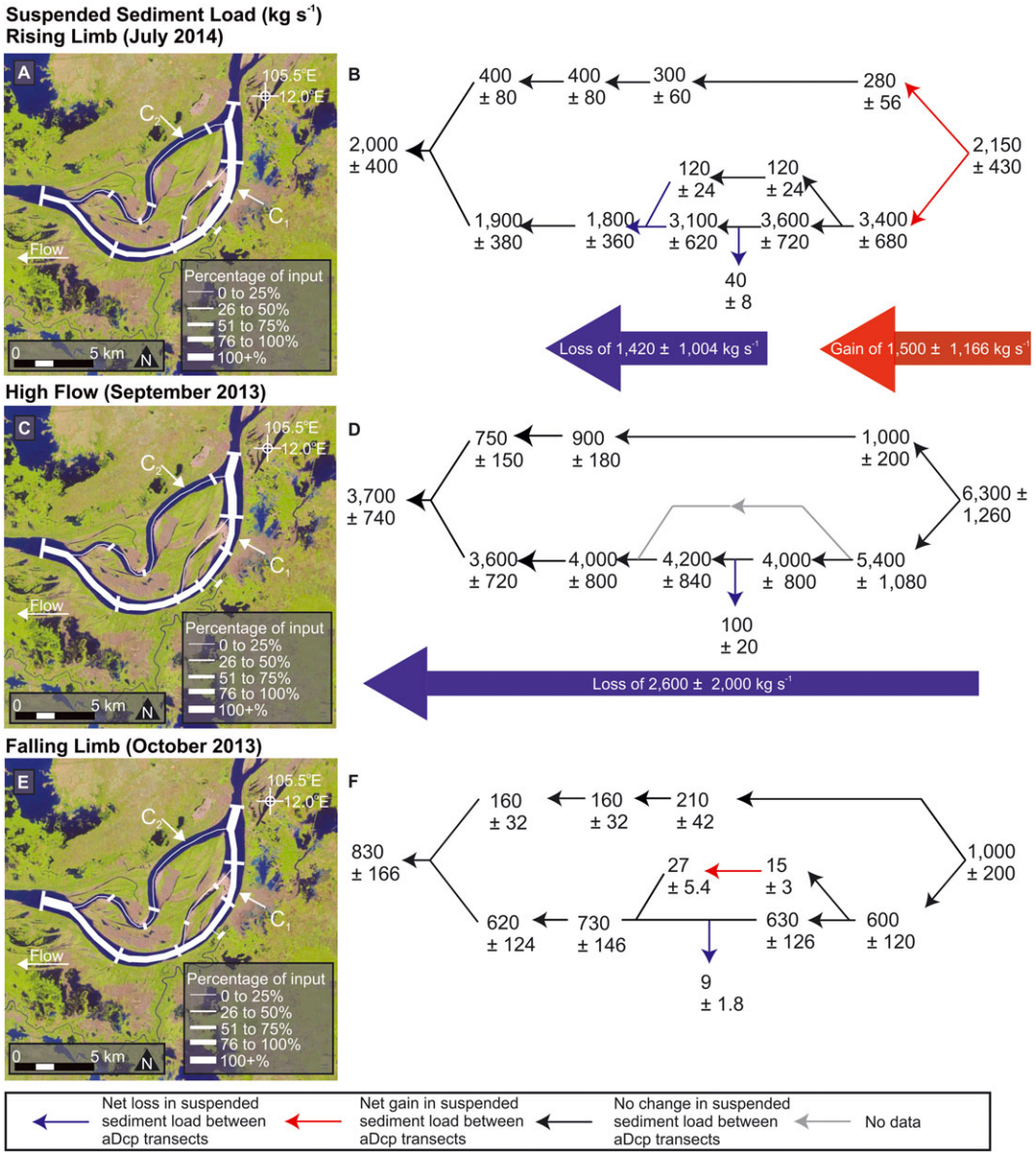

Figure 7. Suspended sediment load (kg s^{-1}) fluctuations through the diffluence–confluence unit. (A, C, E) Flow diagrams with line widths proportional to the suspended sediment load measured at XS001 (upstream extent) overlain on Landsat 8 imagery from October 2013. (B, D, F) Topological representations of suspended sediment load through the diffluence–confluence unit on the rising limb, high flows and falling limbs, respectively. Links with gains (red), losses (blue), no change (black) and no data (grey) are identified. Errors provided are 20% of the value, equivalent to 1 standard deviation of the sediment load calculated from the repeat transects taken at XS001 (see text for details). The large arrows beneath subplots (B), (D) and (F) represent links with significant gains (red) or losses (blue) where appropriate. [Colour figure can be viewed at wileyonlinelibrary.com]

$\pm 1166\,\mathrm{kg\ s^{-1}}$ of additional sediment was remobilized as suspended load between XS001 and XS002, around the bar head on C_1. This additional suspended load persisted until XS004A, after which a decrease of $1420 \pm 1004\,\mathrm{kg\ s^{-1}}$ was recorded (Figures 7A and 7B). However, taken over the course of the entire diffluence–confluence unit the sediment flux appears to be in balance, with deposition at the island head approximately balancing erosion at the tail of the island, and no significant net loss or gain of suspended sediment between the upstream bifurcation and downstream confluence.

During high flows, a sediment flux of $6300 \pm 1260\,\mathrm{kg\ s^{-1}}$ was measured entering the diffluence–confluence unit whereas $3700 \pm 740\,\mathrm{kg\ s^{-1}}$ exited the reach at XS007. This represents a transmission loss of $2600 \pm 2000\,\mathrm{kg\ s^{-1}}$ (41%) across the unit. As can be seen in Figures 7C and 7D, this loss was systematic down both C_1 and C_2 (specifically, the downstream portion of C_2) although between each individual link in the unit no loss exceeds its error; it is only the summative loss between XS001 and XS007 that shows a significant loss of suspended sediment. Although no significant losses exist throughout the unit, potential hotspots of sediment deposition can be postulated, most notably between XS002 and XS003A on C_1 where $\sim 1400 \pm 1880\,\mathrm{kg\ s^{-1}}$ was lost. This location is the site of a smaller bifurcation within C_1 (see Figure 1A). No measurements were possible within the subsidiary channels at this flow stage (due to the shallow water preventing access by the survey vessels), so we are unable to directly assess the distribution of suspended sediment at this specific bifurcation. However, this region is characterized by well-developed bar head deposits (see satellite images in Figures 1A, 6 and 7), so it is possible that sediment was being deposited on the bar head at this location during this period. Frederici and Paola (2003) and Bolla Pittaluga *et al.* (2003) found that stable bars form at bifurcations with high Shields numbers. Data from XS002 and XS003A suggest that between these two transects there is a large increase in the Shields number (θ), here defined as

$$\theta = \frac{\tau}{(\rho_s - \rho) g D_{50}} \tag{6}$$

where τ is the bed shear stress ($\mathrm{N\ m^{-2}}$), ρ_s is the density of the sediment ($\mathrm{kg\ m^{-3}}$), ρ is the water density ($\mathrm{kg\ m^{-3}}$), g is acceleration due to gravity ($9.81\,\mathrm{m\ s^{-2}}$) and D_{50} is the median bed grain size (0.002 m), with θ increasing from 0.09 to 2.1. We note that our estimates of the Shields parameter have an error of ~13% resulting from the use of aDcp velocity data to calculate τ and in the particle size analysis (~3%; manufacturer specification for Saturn Digisizer).

It is possible that the development of a bar in the bifurcation just upstream of XS003A may account for the loss in suspended sediment through this section. An alternative possibility is that the suspended sediment may be being preferentially partitioned down the smaller bifurcate channel. However, this is unlikely as, when the smaller bifurcate rejoins the main channel (just below XS004A; see Figure 1A), there is no commensurate increase in suspended sediment load at XS005 (Figures 7C and 7D). Similarly, as little sediment was lost between XS003A and XS004A (Figures 7C and 7D), it is more likely that sediment was being deposited around the bifurcation between XS002 and XS003A, perhaps in bar head deposits.

Analysis of the mean annual flow hydrograph at Kampong Cham (Figure 1B) reveals that flows in excess of $27\,000\,\mathrm{m^3\ s^{-1}}$ occur for approximately 78 days a year. Assuming that the sediment loss of $2600 \pm 2600\,\mathrm{kg\ s^{-1}}$ is maintained over those 78 days, the average volume of sand lost at this location would amount to at least $63\,882\,\mathrm{m^3}$ (based on a density of sand of $1920\,\mathrm{kg\ m^{-3}}$). The area of the study reach (the diffluence–confluence unit) as measured from Landsat imagery is $\sim 33\,\mathrm{km^2}$ (Figure 8B). The volumetric sand loss therefore equates to a 0.002 m deposit of sediment uniformly spread across the confluence–diffluence unit during an 'average' flood season. However, as we show in Figure 7, the deposition is not uniform and therefore depths of deposits are likely to be higher in some locations. For example, assuming deposition only occurs in the area of bar head deposits between XS002 and XS003A (shown to be a sink in Figure 7), this area of $1.9\,\mathrm{km^2}$ would experience a deposit depth of 3 cm if all sediment was deposited here across a flood season.

A further potential sink of suspended sediment at high flows appears at the downstream end of the reach, with $400 \pm 1520\,\mathrm{kg\ s^{-1}}$ being lost between XS005 and XS006. The aerial images reveal no obvious bar deposits in this vicinity (Figure 1A). To assess whether material was being stored in this potential sink zone, selected georeferenced aerial photos from 1959 and Landsat images over the period 1973–2013 (selected on the basis of being cloud free and all being taken within the same calendar month to ensure similar flow stage) were analysed and the areal extent of the island complex was delineated (Figure 8). This analysis shows that the island complex has been prograding at its downstream extent at a rate of approximately $0.05\,\mathrm{km^2\ a^{-1}}$ since 1973 ($R^2 = 0.4$. $p = 0.5$; Figure 8). This prograding area corresponds to the region between cross-section XS006 and XS007 and thus precisely to the zone where, at high flows, a sink of suspended sediment was inferred. Therefore, it is likely that this sink zone is actively depositing when flow stage is greater than the mean annual flow ($\sim 14\,500\,\mathrm{m^3\ s^{-1}}$), causing the downstream progradation of the island complex.

During the falling limb of the hydrograph, $1000 \pm 200\,\mathrm{kg\ s^{-1}}$ of sediment was estimated to be entering the unit, with 830

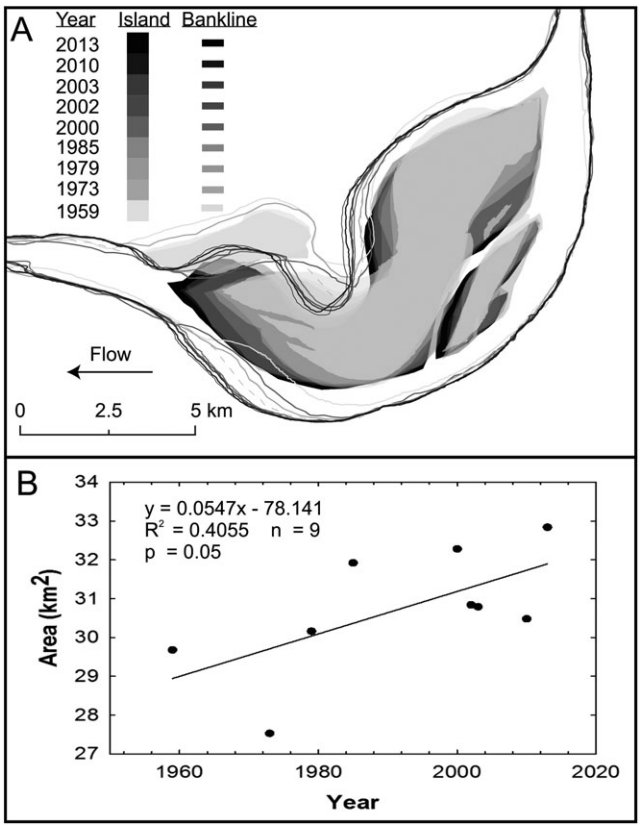

Figure 8. (A) Island areal extents and banklines determined from Landsat imagery over the period 1959–2013. (B) Total area covered by the island complex as a function of year calculated from the areas masked in the Landsat imagery depicted in panel (A), showing average annual aggradation/progradation of $0.05\,\mathrm{km^2}$ a year.

$\pm 166\,kg\,s^{-1}$ exiting at its southernmost extent. This represents a net loss of 17% of the incoming sediment load ($170 \pm 366\,kg\,s^{-1}$). At this flow stage, both C_1 and C_2 display relatively stable links in its downstream extent, with the largest gain of $13 \pm 8.4\,kg\,s^{-1}$ occurring between XS003B and XS004B. This gain is likely associated with a remobilization of sediment sequestered into this smaller subsidiary channel during the higher flow flood period.

Discussion

The results shown in Figure 7 suggest that different regions of the diffluence–confluence unit become active at different flow stages and that individual links within the unit may display different behaviour (net erosion and net deposition) at different flow stages. These differences are likely to be in part controlled by the partitioning of the flow and sediment at the bifurcation at the head of the diffluence–confluence unit, as variations here will impact morphodynamics downstream. To assess how this partitioning varies with flow stage we define the discharge asymmetry ratio of the bifurcation (Q_{r^*}) following Kleinhans *et al*. (2013) such that.

$$Q_{r^*} = \frac{(Q_1 - Q_2)}{Q_0} \tag{7}$$

where Q_0 is the discharge in the main channel upstream of the bifurcation. As values of Q_{r^*} tend towards unity, the distribution of water at the bifurcation becomes more uneven, with more flow discharge being routed down the primary channel (C_1) of the bifurcation. As values approach zero, flow discharge is evenly split between the channels.

Our data show that the discharge asymmetry ratio declined from a value of $Q_{r^*} = 0.54$ during the high flow of the monsoon flood pulse (September 2013, $Q = 27\,000\,m^3\,s^{-1}$), to $Q_{r^*} = 0.44$ on the falling limb of the hydrograph (October 2013, $Q = 13\,500\,m^3\,s^{-1}$), and subsequently rose to a value of 0.59 on the following rising limb of the hydrograph (July 2014; $Q = 19\,500\,m^3\,s^{-1}$). This suggests that the Q_{r^*} fluctuates with discharge and between flood events, with the low flow period between October 2013 and July 2014 representing a time when the bifurcation becomes more unstable (Q_{r^*} values increase towards unity). It also suggests that over the course of the flood (September 2013 and October 2013) the flow partitioning within the bifurcation becomes more symmetrical (i.e. Q_{r^*} values tend closer towards zero). Zolezzi *et al*. (2006) and Szupiany *et al*. (2012) also report that bifurcations tend to become more symmetrical as discharge increases. Our data show that bifurcations become more symmetrical across a single flood wave with increasing discharge, but that this symmetry does not necessarily track variations in flow discharge in a straightforward manner. For example, discharges were higher in July 2014 ($19\,500\,m^3\,s^{-1}$) than in October 2013 ($13\,500\,m^3\,s^{-1}$), but asymmetry was greater for the higher magnitude of the two flows ($Q_{r^*} = 0.59$ compared to 0.44). Furthermore, comparison with the data in Figure 7 suggests that a more equal split of discharge down each bifurcate channel (October 2013; $Q_{r^*} = 0.44$) results in less variation in the suspended sediment budget through the diffluence–confluence unit (Figure 7) that when discharge asymmetry is greater. As discharge is partitioned more unequally, localized zones of erosion and deposition begin to become active throughout the diffluence–confluence unit (Figure 7). Therefore, the initial distribution of discharge at the bifurcation likely plays a key role in determining the behaviour of the unit downstream.

The distribution of discharge between the two channels of a bifurcation has been shown to be controlled by cross-stream water surface slopes (Zolezzi *et al.,* 2006; Szupiany *et al.,* 2012), bed slope (Kleinhans *et al.,* 2008; Hardy *et al.,* 2011) and upstream curvature (Kleinhans *et al.,* 2008; Thomas *et al.*, 2011; Marra *et al*., 2014) amongst many other factors. The results presented above allow us to assess the role of these factors on a large river bifurcation. As discussed above, variations in cross-stream water surface slope are present between the surveys (Figure 4A). We find that the lowest water surface slopes ($3 \times 10^{-5}\,m\ m^{-1}$; October 2013; $Q = 13\,500\,m^3\,s^{-1}$) correspond to the most equal distribution of discharge at the bifurcation ($Q_{r^*} = 0.44$). However, although water surface slopes increase with discharge it does not follow that an increase in water surface slope leads to more unequal partitioning of discharge at the bifurcation. During the highest flows observed (September 2013; $Q = 27\,000\,m^3\,s^{-1}$), water surface slopes were $8 \times 10^{-5}\,m\ m^{-1}$, whereas in July 2014, when $Q = 19\,500\,m^3\,s^{-1}$, water surface slopes were $4 \times 10^{-5}\,mm^{-1}$. However, Q_{r^*} during September 2013 equated to 0.54, whereas in July 2014 Q_{r^*} equated to 0.59. Thus the highest water surface slopes do not correspond to the greatest asymmetry in flow. It is therefore likely that the bed morphological changes shown in Figure 5 that occurred between October 2013 and July 2014 result in a topographic steering of the flow that dominates over the cross-stream water slope with respect to the distribution of the water and sediment between the two bifurcate channels.

The morphological changes may then impact on future distributions of water and sediment through the bifurcating channels, and in doing so potentially shift the bifurcation towards a different equilibrium state. In both fine-grained and coarse-grained systems, the equilibrium configuration of bifurcations has been estimated using numerical modelling techniques (Bolla Pittaluga *et al.,* 2003; Edmonds and Slingerland, 2008; Bolla Pittaluga *et al.,* 2015), though available field data to test these theories have, as discussed previously, to date been lacking. The availability of our field data therefore provides an opportunity to compare the stability diagrams produced from these theoretical studies with real-world data, provided the dimensional and non-dimensional parameter space observed in the real-world data conforms to that used in the numerical studies. For example, the stability curve of Bolla Pittaluga *et al*. (2003) was derived with a half width–depth ratio, β, of 8 and a dimensionless Chezy coefficient, C_a, of 12.5, where the non-dimensional Chezy coefficient is defined following Bolla Pittaluga *et al*. (2015) such that

$$C_a = 6 + 2.5 \log\left(\frac{d}{2.5 D_{50}}\right) \tag{8}$$

where d is the channel depth (m).

For the cross-section at the head of the bifurcation on the Mekong, values of C_a vary from 15 (September 2013) to 17 (October 2013 and July 2014). The respective values of β are approximately 25 across all three survey periods. These values mean that it is not valid to compare the data for the Mekong to the stability curves proposed by Bolla Pittaluga *et al*. (2003) or Edmonds and Slingerland (2008), both of which have similar parameter values ($C_a = 12.5$, $\beta = 8$). However, it is possible to compare our observed data to the stability criteria proposed in Bolla Pittaluga *et al*. (2015), whose stability phase space contains multiple curves for varying values of β. Indeed, one such curve in their phase space equates to $\beta = 25$. Values of C_a for these curves equal 13, and although this is not exactly identical to the values observed for the Mekong (15–17), it is a closer fit to the observed data than other available stability diagrams. Furthermore, Bolla Pittaluga *et al*. (2015) suggest that their stability

relationships are only slightly sensitive to variations in C_a. Therefore, it is reasonable to compare our observed data to this proposed stability curve. Furthermore, we acknowledge that these stability diagrams are also based on the assumption of downstream equal width channels, whereas on the Mekong we observe downstream channels of unequal width ($C_1 = 1400$ m wide, $C_2 = 700$ m wide). Miori *et al.* (2006) explore the effect of removing the assumption of equal downstream channel widths on the stability phase space, demonstrating that the qualitative behaviour tending towards equilibrium is not affected by varied width channels, though the time taken to reach that stable state is affected. As we are not looking at a long temporal sequence of bifurcation stability but, rather, snapshots across a single flood wave, it is again justifiable to compare the Mekong to the stability phase space of Bolla Pittaluga *et al.* (2015).

The behaviour of the Mekong bifurcation when plotted against the Bolla Pittaluga *et al.* (2015) stability diagrams (Figure 9) depends upon the sediment transport regime (bedload or suspended load) dominant at the bifurcation. Bolla Pittaluga *et al.* (2015) define stability phase spaces for both bedload and suspended load dominant systems, using the Van Rijn (1984) sediment transport equation (Figure 9A) for suspended load and a combination of the Meyer-Peter–Müller (MPY; 1948) regime for gravel beds and the Engelund and Hansen (1967) sand bed relationship (Figure 9B) for bedload transport regimes. Assuming for the moment a suspended sediment dominant scenario (Figure 9A), our field data indicate that at the lowest discharge (October 2013; $Q = 13\ 500\ m^3\ s^{-1}$) the bifurcation is in fact in an equilibrium configuration (as defined by Bolla Pittaluga *et al.,* 2015). At the highest observed discharge (September 2013; $Q = 27\ 000\ m^3\ s^{-1}$) the bifurcation is again within the stable phase space proposed by Bolla Pittaluga *et al.* (2015) due to the considerably lower Shields number for the value of Q_{r^*} observed. This reflects the coarsening of the bed material observed at this flow, increasing from medium sand (~0.4 mm) on the rising and falling limbs, to coarse sand (2 mm) during high flows, and therefore likely a transition away from suspended sediment dominant conditions. On the rising limb (July 2014; $Q = 19\ 500\ m^3\ s^{-1}$), the bifurcation transitions into the unstable phase space due to an increase in Shields number that is not matched by an increase in discharge asymmetry. This behaviour is corroborated by our field observations of suspended sediment load through the diffluence–confluence unit, which shows significant net erosion and deposition of suspended sediment only during the rising limb of the hydrograph (Figure 7B).

Conversely, if we assume the bifurcation operates under a bedload-dominated scenario (Figure 9B), the bifurcation is predicted to behave similarly, although it never fully transitions into an unstable phase space. During high flows (September 2013; $Q = 27\ 000\ m^3\ s^{-1}$) the bifurcation is predicted to be in a stable state, transitioning first to the unstable phase space at low flow (October 2013; $Q = 13\ 500\ m^3\ s^{-1}$), before transitioning back to the boundary of the stable–unstable phase space during the rising limb (July 2014; $Q = 19\ 500\ m^3\ s^{-1}$). This pattern conforms to that reported by Zolezzi *et al.* (2006) and Szupiany *et al.* (2012), who propose more stable bifurcations at higher discharges. It is noteworthy that the highest flow discharge we observed ($27\ 000\ m^3\ s^{-1}$) is still just ~50% of the mean annual peak flood value ($52\ 500\ m^3\ s^{-1}$).

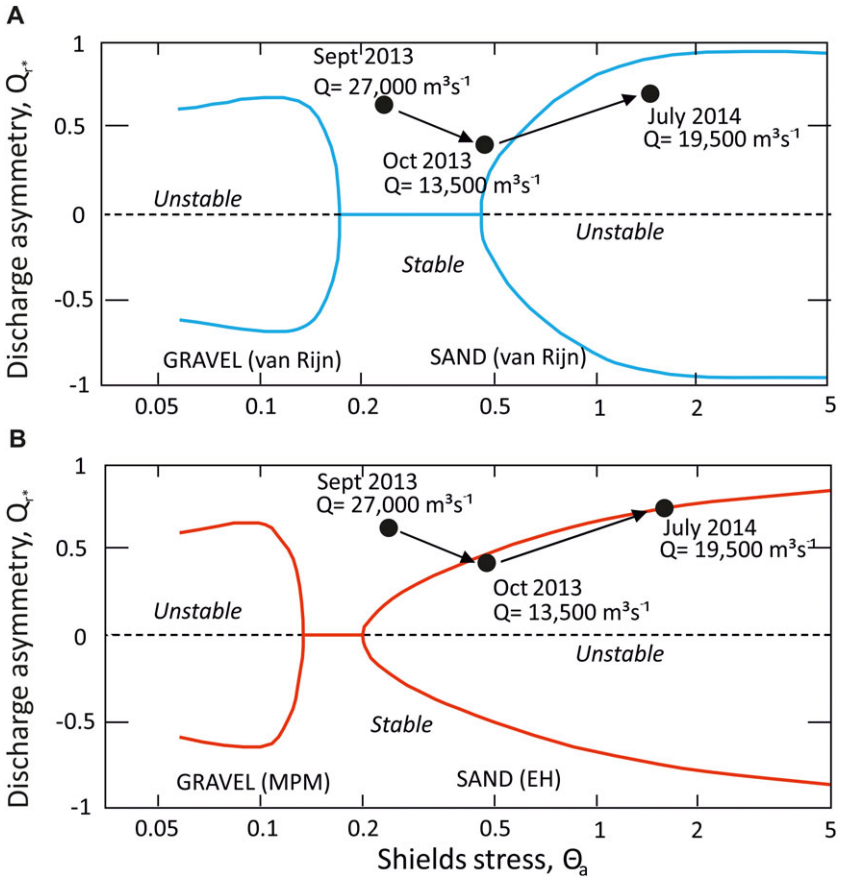

Figure 9. Equilibrium configurations of sand bed and gravel bed bifurcations from Bolla-Pittaluga *et al.* (2015; modified from their Figures 3a and b) for $\beta_a = 50$ under (A) a suspended sediment-dominant regime calculated using the van Rijn (1984) formulation and (B) a bedload sediment-dominant regime calculated using the Meyer-Peter and Müller (1948) and Engelund and Hansen (1967) formulations for gravel bed and sand bed rivers, respectively. Calculated discharge asymmetry ratios and Shields stresses for the three survey periods of the Mekong bifurcation are superimposed as black filled circles with discharges labelled. The arrows depict the temporal trend in the observed data. [Colour figure can be viewed at wileyonlinelibrary.com]

Nevertheless, given the average annual discharge at Kampong Cham is 14 500 $m^3 s^{-1}$, it is likely that the bifurcation that is the specific focus of this study spends the majority of time in a near-stable configuration, regardless of the dominant transport regime. This may suggest that large river bifurcations may form profiles at near-equilibrium configurations at mean-to-low flows, which are the most common throughout the hydrograph. Edmonds and Slingerland (2008) note that stable fine-grained bifurcations are resistant to perturbations, returning to an equilibrium configuration over time. The mode of dominant sediment transport (bedload versus suspended load) has long been identified as a control on river morphology (Schumm, 1985; Church, 2006) and recent modelling work has highlighted the key role suspension of bed material plays in defining large river channel planforms (Nicholas, 2013). Our observations suggest that under differing dominant regimes the bifurcation will behave differently; therefore, understanding the dominant mode of sediment transport in large rivers is key to understanding and predicting large river bifurcation stability and larger planform change, over longer time frames.

Conclusion

This paper reports observations from a bifurcation and associated diffluence–confluence unit on a reach of one of the world's largest rivers: the Mekong in Cambodia. Through the use of high-resolution aDcp flow monitoring and MBES bathymetric surveys across the flood wave, we reveal that bifurcation discharge asymmetry falls from 0.54 at high flows (27 000 $m^3 s^{-1}$) in September 2013 to 0.44 during the falling limb of the flood in October 2013 (13 500 $m^3 s^{-1}$), but increasing back up to 0.59 in July 2014 (19 500 $m^3 s^{-1}$). Our results reveal that flow discharge is not the sole control on bifurcation asymmetry; rather, fluctuations in bifurcation asymmetry appear to be the result of multiple processes operating in tandem, including varying flow discharge, bed morphological change and the influence of cross-stream water surface slopes. The influence of flow discharge is more keenly expressed throughout the diffluence–confluence unit downstream of the bifurcation, where the island complex acts as a sink of suspended sediment during high flows (with a net loss of 2600 ± 2000 kg s^{-1}), but appears to be in quasi-equilibrium distribution during the rising and falling stages. We show that large river bifurcation stability is dependent on the dominant sediment transport regime (bedload versus suspended load) and that transitions to instability occur at different points on the hydrograph dependent upon the changing relative dominance of the mechanism of transport. A deeper appreciation of the dominant transport mechanisms of the world's largest rivers is therefore necessary in order to better predict and understand their planform change and channel behaviour dynamics.

Acknowledgements——This research was supported by awards NE/JO21970/1, NE/JO21571/1 and NE/JO21881/1 (to Southampton, Exeter and Hull, respectively) from the UK Natural Environment Research Council (NERC). We gratefully acknowledge the assistance of the Mekong River Commission, the Department of Hydrology and Water Resources (DHRW), Cambodia and Mr Ben Savuth, Cpt. Thy and Cpt. Horn, and the DHRW research vessel crews for their assistance and company in the field.

References

Aalto R, Maurice-Bourgoin L, Dunne T. 2003. Episodic sediment accumulation on Amazonian flood plains influenced by El Niño/Southern Oscillation. *Nature* **425**: 493–497.

Aalto R, Lauer JW, Dietrich WE. 2008. Spatial and temporal dynamics of sediment accumulation and exchange along Strickland River floodplains (Papua New Guinea) over decadal-to-centennial timescales. *Journal of Geophysical Research - Earth Surface* **113**: 1–22.

Adamson PT, Rutherford ID, Peel MC, Conlan IA. 2009. The hydrology of the Mekong River. In *The Mekong: Biophysical Environment of an International River Basin*, Campbell IC (ed). Elsevier: Amsterdam; 53–76.

Blanckaert K. 2009. Saturation of curvature-induced sedcondary flow, energy losses, and turbulence in sharp open-channel bends: Laboratory experiments, analysis and modeling. *Journal of Geophysical Research*. https://doi.org/10.1029/2008JF001137.

Bolla Pittaluga M, Repetto R, Tubino M. 2003. Channel bifurcation in braided rivers: equilibrium configurations and stability. *Water Resources Research* **39**: 1–13.

Bolla Pittaluga M, Coco G, Kleinhans MG. 2015. A unified framework for stability of channel bifurcations in gravel and sand fluvial systems. *Geophysical Research Letters* **42**: 7521–7536.

Bridge JS. 1993. The interaction between channel geometry, water flow, sediment transport and deposition in braided rivers. *Geological Society, London, Special Publications* **75**: 13–71.

Carling PA. 2009. The geology of the Lower Mekong River. In *The Mekong: Biophysical Environment of an International River Basin*, Campbell IC (ed). Elsevier: Amsterdam; 13–28.

Church M. 2006. Bed material transport and the morphology of alluvial river channels. *Annual Review of Earth and Planetary Sciences* **34**: 325–354.

Constantine JA, Dunne T, Ahmed J, Legleiter C, Lazarus ED. 2014. Sediment supply as a driver of river evolution in the Amazon Basin. *Nature Geoscience* **7**: 1–23.

Darby SE, Leyland J, Kummu M, Räsänen TA, Lauri H. 2013. Decoding the drivers of bank erosion on the Mekong River: the roles of the Asian monsoon, tropical storms, and snowmelt. *Water Resources Research* **49**. https://doi.org/10.1002/wrcr.20205.

Darby SE, Hackney CR, Leyalnd J, Kummu M, Lauri H, Parsons DR, Best JL, Nicholas AP, Aalto R. 2016. Fluvial sediment supply to a mega-delta reduced by shifting tropical-cyclone activity. *Nature* **539**: 276–279.

Eaton BC, Millar RG, Davidson S. 2010. Channel patterns: braided, anabranching, and single-thread. *Geomorphology* **120**: 353–364.

Edmonds DA, Slingerland RL. 2008. Stability of delta distributary networks and their bifurcations. *Water Resources Research* **44**. https://doi.org/10.1029/2008WR006992.

Engel FL, Rhoads BL. 2016. Three-dimensional flow structure and patterns of bed shear stress in an evolving compound meander bend. *Earth Surface Processes and Landforms*. https://doi.org/10.1002/esp.3895.

Engelund F, Hansen E. 1967. A monograph on sediment transport in alluvial streams. In *Report, Technical University of Denmark*. Copenhagen: Technisk Forlag.

Frederici B, Paola C. 2003. Dynamics of channel bifurcations in noncohesive sediments. *Water Resources Research* **39**: 6. https://doi.org/10.1029/2002WR001434.

Gupta A, Liew SC. 2007. The Mekong from satellite imagery: a quick look at a large river. *Geomorphology* **85**: 259–274.

Hackney C, Carling PA. 2011. The occurrence of obtuse junction angles and changes in channel width below tributaries along the Mekong River, South-East Asia. *Earth Surface Processes and Landforms* **36**: 1563–1576.

Hardy RJ, Lane SN, Yu D. 2011. Flow structures at an idealized bifurcation: a numerical experiment. *Earth Surface Processes and Landforms* **36**: 2083–2096.

Kleinhans MG, Jagers HRA, Mosselman E, Sloff CJ. 2008. Bifurcation dynamics and avulsion duration in meandering rivers by one-dimensional and three-dimensional models. *Water Resources Research* **44** W08454, https://doi.org/10.1029/2007WR005912.

Kleinhans MG, Ferguson RI, Lane SN, Hardy RJ. 2013. Splitting rivers at their seams: bifurcations and avulsion. *Earth Surface Processes and Landforms* **38**: 47–61.

Kostaschuk R, Best J, Villard P, Peakall J, Franklin M. 2005. Measuring flow velocity and sediment transport with an acoustic Doppler current profiler. *Geomorphology* **68**: 25–37.

Kummu M, Lu XX, Rasphone A, Sarkkula J, Koponen J. 2008. Riverbank changes along the Mekong River: remote sensing detection in the Vientiane–Nong Khai area. *Quaternary International* **186**: 100–112.

Lane SN, Bradbrook K, Richards KR, Biron PM, Roy AG. 2000. Secondary circulation cells in river channel confluences: measurement artefacts or coherent flow structures? *Hydrological Processes* **14**: 2047–2071.

Latrubesse EM. 2008. Patterns of anabranching channels: the ultimate end-member adjustment of mega rivers. *Geomorphology* **101**: 130–145.

Leopold LB, Wolman MG. 1957. *River Channel Patterns: Braided, Meandering and Straight*. USGS: Washington, DC.

Marra WA, Parsons DR, Kleinhans MG, Keevil GM, Thomas RE. 2014. Near-bed and surface flow division patterns in experimental river bifurcations. *Water Resources Research* **50**: 1506–1530.

McLelland SJ, Ashworth PJ, Best JL, Roden J, Klaassen GJ. 1990. Flow structure and transport of sand-grade suspended sediment around an evolving braid bar, Jamuna River, Bangladesh. In *Fluvial Sedimentology VI*, Smith ND, Rogers J (eds). International Association of Sedimentologists: Gent, Belgium; 43–57.

Meyer-Peter E, Müller R. 1948. Formulas for bedload transport. In *Proceedings of the Second International Association of Hydraulic Structures Research Congress*, Stockholm; 3203–3212.

Milliman JD, Farnsworth KL. 2011. *River Discharge to the Global Ocean: A Global Synthesis*. Cambridge University Press: Cambridge, UK.

Milliman JD, Syvitski JPM. 1992. Geomorphic/tectonic control of sediment discharge to the ocean: the importance of small mountainous rivers. *Journal of Geology* **100**: 525–544.

Miori S, Repetto R, Tubino M. 2006. A one-dimensional model of bifurcations in gravel bed channels with erodible banks. *Water Resources Research*: 42. https://doi.org/10.1029/2006WR004863.

MRC. 2009. *The Flow of the Mekong*. Vientiane: Mekong River Commission Secretariate.

Mueller DS, Wagner CR. 2009. Measuring discharge with acoustic Doppler current profilers from a moving boat. In *US Geological Survey Techniques and Methods 3A-22*. Reston, VA: USGS.

Nicholas AP. 2013. Morphodynamic diversity of the world's largest rivers. *Geology* **41**: 475–478.

Parker G. 1991. Selective sorting and abrasion of river gravel. II. Applications. *Journal of Hydraulic Engineering, ASCE* **117**: 150–171.

Parsons DR, Best JL, Lane SN, Orfeo O, Hardy RJ, Kostaschuk R. 2007. Form roughness and the absence of secondary flow in a large confluence–diffluence, Rio Paraná, Argentina. *Earth Surface Processes and Landforms* **32**: 155–162.

Parsons DR, Jackson PR, Czuba JA, Engel FL, Rhoads BL, Oberg KA, Best JL, Mueller DS, Johnson KK, Riley JD. 2013. Velocity Mapping Toolbox (VMT): a processing and visualization suite for moving-vessel ADCP measurements. *Earth Surface Processes and Landforms* **38**: 1244–1260.

Richardson WR, Thorne CR. 2001. Multiple thread flow and channel bifurcation in a braided river: Brahmaputra-Jamuna River, Bangladesh. *Geomorphology* **38**: 185–196.

Schumm SA. 1985. Patterns of alluvial rivers. *Annual Review of Earth and Planetary Sciences* **13**: 5–27.

Shugar DH, Kostaschuk R, Best JL, Parsons DR, Lane SN, Orfeo O, Hardy RJ. 2010. On the relationship between flow and suspended sediment transport over the crest of a sand dune, Rio Parana, Argentina. *Sedimentology* **57**: 252–272.

Szupiany RN, Amsler ML, Best JL, Parsons DR. 2007. Comparison of fixed- and moving-vessel flow measurements with an aDp in a large river. *Journal of Hydrologic Engineering* **133**: 1299–1309.

Szupiany RN, Amsler ML, Parsons DR, Best JL. 2009. Morphology, flow structure, and suspended bed sediment transport at two large braid-bar confluences. *Water Resources Research* **45** W05415, https://doi.org/10.1029/2008WR007428.

Szupiany RN, Amsler ML, Hernandez J, Parsons DR, Best JL, Fornari E, Trento A. 2012. Flow fields, bed shear stresses, and suspended bed sediment dynamics in bifurcations of a large river. *Water Resources Research* **48**: 1–20.

Thomas RE, Parsons DR, Sandbach SD, Keevil GM, Marra WA, Hardy RJ, Best JL, Lane SN, Ross JA. 2011. An experimental study of discharge partitioning and flow structure at symmetrical bifurcations. *Earth Surface Processes and Landforms* **36**: 2069–2082.

van Rijn LC. 1984. Sediment transport part II: Suspended load transport. *Journal of Hydraulic Engineering* **110**: 1431–1456.

Whiting PJ, Dietrich WE. 1990. Boundary shear stress and roughness over mobile alluvial beds. *Journal of Hydraulic Engineering, ASCE* **116**: 1495–1511.

Zolezzi G, Bertoldi W, Turbino M. 2006. Morphological analysis and prediction of river bifurcations. In *Braided Rivers: Processes, Deposits, Ecology and Management*, Sambrook Smith GH, Best JL, Bristow CS, Petts GE (eds). Special Publication 36. International Association of Sediment: Malden, MA; 233–256.

